



Magnetically activated 3D printable polylactic acid/polycaprolactone/magnetite composites for magnetic induction heating generation

Itziar Galarreta-Rodriguez^{1,2} · Alberto Lopez-Ortega^{1,2} · Eneko Garayo^{1,2} · Juan Jesús Beato-López^{1,2} · Paulo La Roca^{1,2,3} · Vicente Sanchez-Alarcos^{1,2} · Vicente Recarte^{1,2} · Cristina Gómez-Polo^{1,2} · Jose Ignacio Pérez-Landazábal^{1,2}

Received: 26 December 2022 / Revised: 2 May 2023 / Accepted: 6 May 2023
© The Author(s) 2023

Abstract

Additive manufacturing technology has attracted the attention of industrial and technological sectors due to the versatility of the design and the easy manufacture of structural and functional elements based on composite materials. The embedding of magnetic nanoparticles in the polymeric matrix enables the development of an easy manufacturing process of low-cost magnetically active novel polymeric composites. In this work, we report a series of magnetic composites prepared by solution casting method combining 5 to 60 wt.% of 140 ± 50 nm commercial Fe_3O_4 nanoparticles, with a semi-crystalline, biocompatible, and biodegradable polymeric blend made of polylactic acid (PLA) and polycaprolactone (PCL). The composites were extruded, obtaining 1.5 ± 0.2 mm diameter continuous and flexible filaments for fused deposition modelling 3D printing. The chemical, magnetic, and calorimetric properties of the obtained filaments were investigated by differential scanning calorimetry, thermogravimetric analysis, magnetometry, and scanning electron microscopy. Furthermore, taking advantage of the magnetic character of the filaments, their capability to generate heat under the application of low-frequency alternating magnetic fields (magnetic induction heating) was analyzed. The obtained results expose the versatility of these easy manufacturing and low-cost filaments, where selecting a desired composition, the heating capacity can be properly adjusted for those applications where magnetic induction plays a key role (i.e., magnetic hyperthermia, drug release, heterogeneous catalysis, water electrolysis, gas capture, or materials synthesis).

Keywords Magnetic nanoparticles · Composite materials · Magnetic filaments · Fused deposition modelling · 3D printing

1 Introduction

In recent years, additive manufacturing has attracted the attention of industrial and technological sectors due to the possibility of fabricating objects without shape and size restrictions in an accessible, low-cost, swift, and very

precise way [1, 2]. Additive manufacturing processes involve models, patterns, prototypes, tools, and three-dimensional end products through the automated deposition of materials layer-by-layer. Nowadays, it is possible to manufacture elements composed of polymers [3], metals [4], and/or ceramics [5] with the required geometry according to a simple digital design. Thus, no special tools or pre-formed molds are required for the construction of the final component, which significantly reduces the cost and speeds up the production process. In this regard, fused deposition modelling (FDM) is a well-known 3D printing technique based on low-temperature range (373–523 K) melt extrusion, where thermoplastic materials in the form of filament are used [6]. Due to its low cost, the wide selection of materials, and high precision, it has become one of the most widely used printing techniques worldwide [7]. In addition, FDM 3D printers do not require large or complex equipment and can be configured to operate under low power consumption such

✉ Itziar Galarreta-Rodriguez
itziargalarreta@gmail.com

✉ Alberto Lopez-Ortega
lopezortega.alberto@gmail.com

¹ Departamento de Ciencias, Universidad Pública de Navarra, Campus de Arrosadía, 31006 Pamplona, Spain

² Institute for Advanced Materials and Mathematics (INAMAT2), Universidad Pública de Navarra, Campus de Arrosadía, 31006 Pamplona, Spain

³ Centro Atómico Bariloche (CNEA), CONICET, 8400 Bariloche, Argentina

as renewable solar energy, so they are easily transportable and adaptable to any place in the world [8].

The current exponential growth of 3D printing new technologies has entailed the necessity to develop novel cutting-edge materials with advanced or combined physicochemical properties. In this sense, the need for novel materials with new and improved properties has led to the use of composite materials (CMs) [9, 10]. CMs are formed by mixing two or more materials and are characterized by having superior properties to those of their single components [11]. CMs consist of a matrix, which ensures the cohesion of the material, and a filler, which modifies the properties of the matrix [12]. In this framework, the common base 3D printable raw materials such as polycaprolactone (PCL), polylactic acid (PLA), and acrylonitrile butadiene styrene (ABS) among other biodegradable thermoplastics have been used as matrix due to their low-cost and easy manufacturing properties. Consequently, the nature of the matrix and the filler, their proportions, adhesion, and the production process will mainly determine the final composite characteristics. Specifically, by changing the constituent elements (polymer type, particles, and/or additives), it is possible to modify their physicochemical properties and create new multifunctional materials [13–17].

Specifically, magnetic CMs have acquired an important role due to their diversity of applications in fields such as electronics, aeronautics, environmental remediation, and biomedicine [2, 18–20]. So far, the most common structures based on magnetic CMs fabricated by FDM have been prepared using ferromagnets and/or ferrimagnets [21–23], classified into two main groups: hard and soft magnetic materials. While the former has the ability to remain permanently magnetized and generate magnetic fields in the absence of external stimulus [24], the composites prepared with soft magnetic materials can be easily magnetized in the direction of an external magnetic field and are widely employed as magnetic flux concentrators. In addition, novel magnetic CMs have been recently proposed using superparamagnetic nanoparticles (NPs). These systems display negligible interparticle magnetic interactions since magnetization can randomly flip direction due to thermal contribution. In general, the most commonly used superparamagnetic NPs for the preparation of magnetic CMs are those based on iron oxides [2]. Interestingly, these superparamagnetic nanostructures have been extensively applied in several technological areas with special emphasis on biomedical applications [25–27]. In this aim, superparamagnetic NPs are proposed as contrast agents, image tracers, or local drug carriers due to their high biocompatibility, high magnetic response, and low-cost [28–30]. However, many of these potential uses rely on their ability to absorb energy from an externally applied alternating (AC) magnetic field [31]. This energy eventually heats the nearby tissues (magnetic hyperthermia) or/and triggers

the liberation of drugs carried by the NPs (drug delivery) [32]. On the other hand, this capability has been also proposed in diverse applications such as heterogeneous catalysis [33], water electrolysis [34], gas capture [35], or materials synthesis [36].

Therefore, in this work, we present the fabrication of a low-cost and easy-manufacturing novel magnetic CMs raw material for FDM 3D printing based on PLA and PCL polymeric blend and commercial Fe_3O_4 NPs. Although a few works have studied the possibility to manufacture composites for heat generation, they are based on much more expensive polymers or ceramic materials [16, 37, 37–39]. On the other hand, studies of PLA + Fe_3O_4 [27], PCL + Fe_3O_4 [28], and PLA + PCL [29] can be found in the literature, but the PLA + PCL + Fe_3O_4 ternary composite for heat generation is the first time reported in literature.

A series of different composites (5 to 60 wt.%) have been prepared by solution casting method combining commercial 140 ± 50 nm Fe_3O_4 NPs embedded in a semi-crystalline, biocompatible, and biodegradable polymeric PLA/PCL blend. Furthermore, the composites were extruded, obtaining continuous and flexible filaments (1.5 ± 0.2 mm diameter) and printed with different shapes demonstrating their capabilities to be used in FDM 3D printing technology. A deep characterization has revealed that the NPs concentration affects the properties of the filaments. Taking advantage of the magnetic character of the filaments, their capability to generate heat under the application of low-frequency AC magnetic fields (magnetic induction) was analyzed. Interestingly, it revealed the versatility of the herein proposed material, where selecting a desired filling factor (i.e., the mass fraction of magnetic NPs per mass of composite) in the filaments and correct applied magnetic field frequency and intensity, the heating capacity can be properly controlled.

2 Materials and methods

2.1 Materials

Poly(lactic acid) (PLA, average molecular weight (M_w) $\approx 144,000$) and polycaprolactone (PCL, average molecular weight (M_w) $\approx 50,000$) were purchased from Resinex and Polymorph, respectively. 140 ± 50 nm magnetic iron (II, III) oxide NPs (637,106-100G) and dichloromethane (DCM) solvent were purchased from Sigma Aldrich.

2.2 Preparation of PLA/PCL/ Fe_3O_4 filaments

In order to obtain the 3D printable magnetic filaments, six composites with different amounts of PLA, PCL, and Fe_3O_4 NPs were prepared (Table 1).

Table 1 Summary of the masses of employed components (PLA, PCL, and NPs) and the estimated filling factors obtained from the fabrication procedure, thermogravimetric analysis (TGA), and magnetometry

| Composite | Experimental | | | Filling factor (%) | | |
|-----------|--------------|---------|--|--------------------|-----|--------------|
| | PLA (g) | PCL (g) | Fe ₃ O ₄ NPs (g) | Fabrication | TGA | Magnetometry |
| P0% | 10 | 90 | - | - | - | - |
| P5% | 9.5 | 85.5 | 5 | 5 | 5 | 5 |
| P10% | 9 | 81 | 10 | 10 | 12 | 8 |
| P20% | 8 | 72 | 20 | 20 | 21 | 18 |
| P40% | 6 | 54 | 40 | 40 | 40 | 38 |
| P60% | 4 | 36 | 60 | 60 | 57 | 56 |

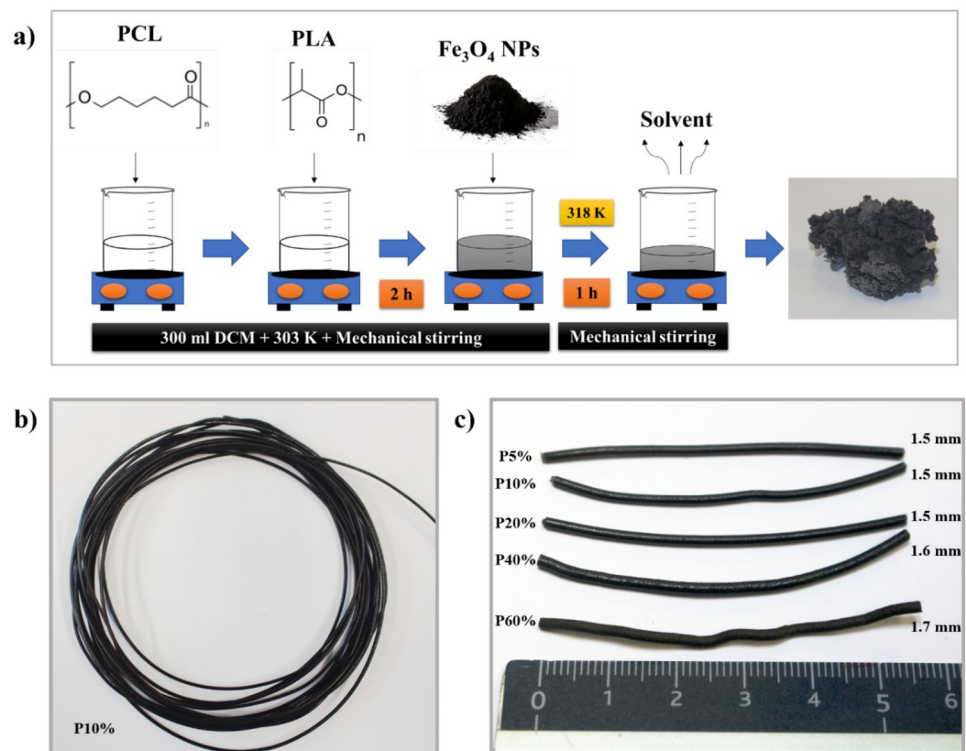
To carry out the preparation of the composites, the following procedure was developed (see Fig. 1): first, 10 g of PLA was dissolved in 300 mL of DCM with mechanical stirring at 303 K. As the PLA was dissolved, the colorless solution become more viscous, and 90 g of PCL was added. To promote a homogeneous mixture between both polymers, the solution was left under constant stirring and temperature for 2 h. After this time, the corresponding quantity of Fe₃O₄ NPs (Table 1) was added and left in constant mechanical stirring for 1 h. Finally, the temperature was increased to 318 K to facilitate the evaporation of the solvent. The NPs percentage in mass (i.e., filling factor) of the prepared composites was adjusted by changing the mass proportions of the polymers and the Fe₃O₄ NPs.

The dried magnetic composite was mechanically extruded to obtain continuous and flexible filaments of 1.5 ± 0.2 mm in diameter for their subsequent use in 3D printing (see Fig. 1b, c). The fabrication of magnetic filaments was

carried out using an extruder (FelFil Evo) with a 1.75-mm circular cross-section nozzle. The extrusion temperature was adjusted between 363 and 423 K depending on the mass percent of NPs and the polymer mixture in the final product composition. However, similar speed extrusion (10 cm/min) was adopted to assemble the magnetic filaments.

2.3 Characterization

Employed commercial iron oxide (Fe₃O₄) particle average size estimation was made by transmission electron microscopy (TEM) measurements in an “FEI TECNAI T20” microscope. The morphologies of the prepared filaments, including the NPs distribution, were investigated by scanning electron microscopy (SEM, Zeiss EVO), high-resolution SEM (HR-SEM, Zeiss GEMINI), and energy dispersive X-ray spectroscopy (EDX).

Fig. 1 a Schematic representation of the composite preparation procedure and b, c extruded magnetic filaments

The thermal stability, thermogravimetric analysis (TGA), of the extruded filaments, was studied using a TGA/DSC 3+ from Mettler Toledo in the range of 193–473 K at a 10 K/min rate in nitrogen flow. Thermal properties were determined by differential scanning calorimetry (DSC) (Q-100 DSC, TA Instruments). The samples were pre-sealed into an aluminum pan, and the analysis was performed in four steps: (i) 1st cooling from 303 to 193 K at 10 K/min, (ii) 1st heating from 193 to 473 K at 10 K/min, (iii) 2nd cooling again to 193 K, and (iv) finally the 2nd heating to 473 K at 10 K/min. The crystallization ($T_{c_{PCL}}$) temperature and crystallization enthalpy per mass ($\Delta H_{c_{PCL}}$) of PCL was determined from the 2nd cooling curve while the melting temperature ($T_{m_{PCL}}$) and melting enthalpy per mass ($\Delta H_{m_{PCL}}$) were determined from the 2nd heating curve. The equivalent characteristic parameters of PLA were determined from the 2nd heating curve: cold crystallization ($T_{cc_{PLA}}$) temperature, cold crystallization enthalpy per mass ($\Delta H_{cc_{PLA}}$), melting temperature ($T_{m_{PLA}}$), and melting enthalpy per mass ($\Delta H_{m_{PLA}}$). Crystallization and melting temperatures were taken at the maximum of the crystallization and the melting peaks, respectively. To average out sample statistical fluctuations, 3 different samples were extracted from the same filament, and the mean value of the characteristic thermal parameters was estimated. Since PCL crystallizes on cooling and PLA on heating, two different equations have been used to calculate the crystallinity degree (χ_c) of both polymers at room temperature. First, the crystallinity degree of PLA was obtained by the following [40, 41]:

$$X_c(\%)_{PLA} = \left(\frac{\Delta H_{m_{PLA}} - \Delta H_{cc_{PLA}}}{\Delta H_{m_0}} \right) \times 100 \quad (1)$$

The crystallinity degree of PCL was calculated by the following [42, 43]:

$$X_c(\%)_{PCL} = \left(\frac{\Delta H_{m_{PCL}}}{\Delta H_{m_0}} \right) \times 100 \quad (2)$$

where $\Delta H_{m_0} = 93,6$ J/g (or 135 J/g) is the melting enthalpy of the 100% PLA (or PCL) [42, 44].

The magnetic characterization of the commercial NPs and the extruded magnetic filaments were analyzed by the magnetic field (H)-dependent magnetization measurements, $M(H)$, on a Quantum Design SQUID magnetometer (QD MPMS XL-7), with a superconducting magnet up to 70 kOe and equipped with a cryostat that can measure from 2 to 400 K. The values of coercive field (H_c), remanence (M_r), magnetization measured at 10 and 300 K at a maximum applied magnetic field of 60 kOe (normalized to the measured composite sample mass), M_s , and reduced remanence ($R = M_r/M_s$) were obtained from the hysteresis loops. The

magnetic hyperthermia experiments were performed using a commercial G3 D5 series Multi-mode 3000W Drive from nanoscale Biomagnetics setup. During these experiments, water and air, surrounding composites were heated by magnetic induction. The increase in temperature was measured by a portable IR Thermal Imager (PCE-TC 33 N) [45] (18–40 mg) for filaments on air whereas a fiber optic thermometer (Neoptix Inc., Canada) in contact with aqueous media (1 mL of deionized water) was used in the case of water surrounded samples. The measurements of dynamic magnetization were carried out in aqueous media (1 mL of deionized water) using a previously tested lab-made AC magnetometer [46]. The heat-generating capability of the filaments, the specific absorption rate (SAR), and generated power density (ρ) were obtained from dynamic magnetization measurements at 311 kHz [47]:

$$\rho = f A = -f \int_{\text{Cycle}} M_t dH_{app} = \frac{\text{Absorbed Power}}{\text{volume}} \quad (3)$$

where f is the AC magnetic field frequency, M_t is the dynamic volumetric magnetization (SI units $A \cdot m^{-1}$), and H_{app} is the applied AC magnetic field intensity. A is the area enclosed by the hysteresis loop measured at frequency f (see Fig. S1). Because SAR is normalized by the mass of NPs, ρ is related with the SAR according to the following [48]:

$$SAR = \frac{\rho}{c} = \frac{\text{Absorbed Power}}{\text{mass NPs}} \quad (4)$$

where c is the total mass of magnetic NPs in the filaments divided by the NPs volume. The absorbed power density defines the maximum temperature (T_{max}) that a composite and the surrounding material (e.g., biological tissues or specific medium) can reach [49]. In the case of a material absorbing energy from an AC magnetic field, T_{max} corresponds to the equilibrium temperature, reached when total power absorbed by the material equals the dissipated power flowing out of the material by thermal conduction, convection, or irradiation.

2.4 3D printability of magnetic filaments

The printing of different shapes and sizes of objects was carried out using an Artillery Sidewinder X1 3D printer based on the FDM technology. In all cases, Open Source-Software CURA 4.12.1 (Ultimaker B.V. Utrecht, Netherlands) was used to format the printing algorithm (layer thickness of 0.3 mm and 100% infill density). A printing temperature of 573 K was employed to print the filaments using a 0.4-mm extruding head. The layer height was 0.3 mm, the speed in the printing movements was 12.5 mm/min, and the bed temperature was 313 K.

3 Results and discussion

A series of five magnetic composites were prepared by solution casting method combining nanometric 140 ± 50 nm commercial magnetic Fe_3O_4 NPs (Fig. S2), with a polymeric blend made of a 10% PLA and 90% PCL (see Fig. 1a).

As previously reported [50, 51], this polymer mixture enhances the structural strength with respect to neat PCL, while keeping the melting temperature around 328 K, enabling the manufacture of filaments flexible enough to be used as raw material for FDM 3D printing. The samples were labeled as P#%, where # represents the percentage of NPs in the composites (from 5 to 60 wt.%).

Figure 2a–c depicts the cross-section SEM images for selected P5%, P20%, and P60% samples. The cross-section SEM images for P5% and P20% samples are represented in Fig. S3a, b. It can be seen that while at low NPs concentrations the filaments show a regular morphology and dense structure, the increase in the magnetic component fosters the deterioration of the morphology. As NPs concentration increases, the filament becomes rougher with a consequent enhancement of the porosity, i.e., porous in the micrometric

range [39, 52–54]. Interestingly, it must be noted that the increased porosity does not affect the macroscopic aspect of the extruded filament, displaying, all the series of composites, a smooth surface (see Fig. 1c). To study the NPs' dispersion into the polymeric matrix, EDX mapping was carried out (see Fig. 2d–f and Fig. S3c, d).

It can be observed that the NPs are well distributed along the whole filament, and, at the same time, for certain series of compositions, the nanostructures tend to form micrometric agglomerates. The homogeneous NPs dispersity was also confirmed by HR-SEM images, which show that most of the particles were individually distributed in the polymeric matrix (see Fig. 2g, h and Fig. S4). In addition, in Fig. 2i, a part of the micrometric porosity, smaller cavities with diameters ranging from 200 to 600 nm were observed in the filament with the highest NPs loading.

To investigate the effect of the NPs concentration on the thermal properties of the magnetic filaments, TGA curves were obtained for the whole series of composites; two distinct weight losses corresponding to each polymer decomposition can be observed (see Figs. 3 and S5).

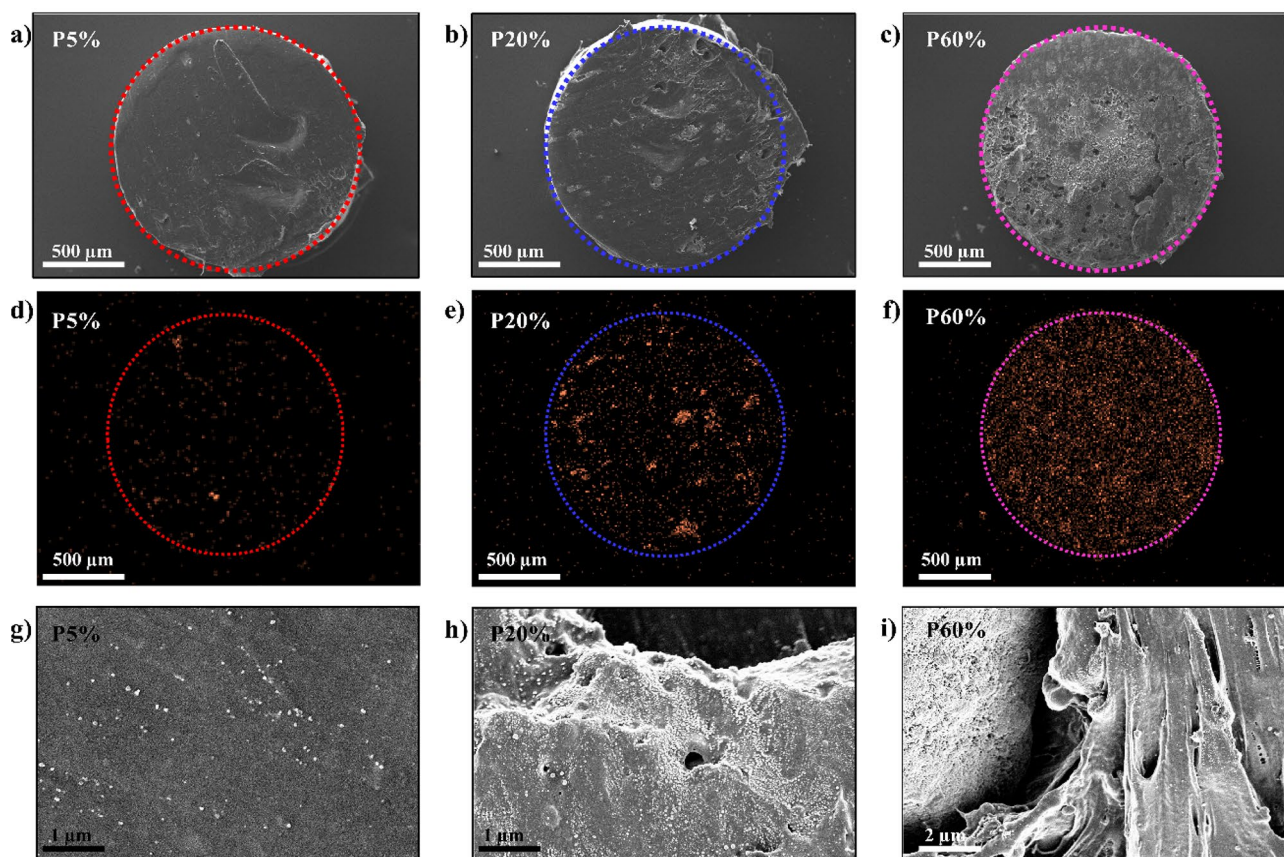


Fig. 2 SEM images and corresponding composite EDX maps of the magnetic filament cross section for **a**, **d** P5%; **b**, **e** P20%; and **c**, **f** P60% samples (orange color in **d**, **e** and **f** corresponds to the Fe absorption

edge). HR-SEM images of selected regions of the composite for **g** P5%, **h** P20%, and **i** P60% samples

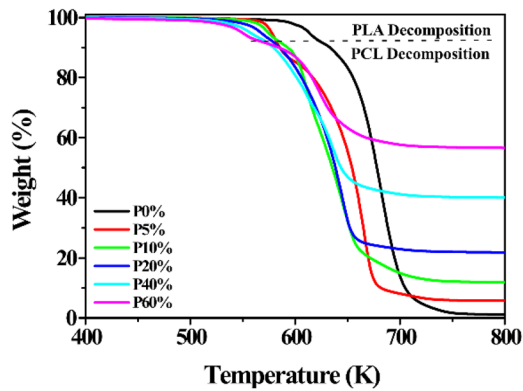


Fig. 3 TGA curves for the series of magnetic filaments

Since the PLA decomposes at lower temperatures than PCL (i.e., 641 and 688 K, respectively), the first weight loss was employed to determine the amount of PLA in the sample, while the second one enabled the determination of the mass of PCL. Fe_3O_4 NPs content can be determined as the remnant mass percentage at the end of the thermal scan. Table 1 and Fig. S5 depict the estimated polymer content and the magnetic NPs percentage for each sample. The obtained results are in good agreement with the expected values considering the employed percentages of each component in the composites' preparation. Moreover, it should be noticed that the introduction of magnetic NPs causes an overall reduction of the decomposition temperature of the polymeric blend, enhanced by the increase in the NP filling factor. Specifically, it is observed that the decomposition of both polymers is shifted towards lower temperatures with increasing Fe_3O_4 wt.%. This is in good agreement with previously reported works [55], where the increase in the pyrolysis of PCL chains is linked to the incorporation of magnetic NPs due to the limitation of the movement of polymeric chains [56, 57]. At the same time, water that might be adsorbed on the surface of the NPs could act as depolymerization catalysts and accelerate the degradation of both polymers [58]. Despite this decrease in the decomposition temperatures, it is worth noting that the degradation onset

for all the filaments is above the usually used printing temperature (473 K), which ensures the viability of the composites for FDM 3D printing.

Furthermore, as previously described in the experimental procedure, the filaments were subjected to four thermal scans. The 1st cooling and heating scans (303 K to 353 K and 353 K to 473 K, respectively) were mainly employed to erase the previous thermal history of the prepared filaments. Figure 4a, b show the following 2nd cooling and heating scans.

The exothermic peak in the cooling curve of the PCL displayed in Fig. 4a can be associated with the PCL crystallization (T_{cPCL}). The following heating scan depicted in Fig. 4b allows the determination of the melting temperature of PCL, T_{mPCL} , and the subsequent crystallization, T_{ccPLA} , and melting temperature, T_{mPLA} , of PLA [59]. Due to PLC/PLA immiscibility, the thermal transitions in each polymer are clearly visible independently [60, 61]. Table 2 summarizes the estimated characteristic temperatures from the DSC scans as a function of the NPs percentage.

As can be seen in Table 2, T_{mPCL} and T_{cPCL} do not seem to be affected by the presence of PLA polymer or NPs, while T_{mPLA} and T_{ccPLA} decrease as the filling factor increases. As previously reported [62], this variation in T_{ccPLA} could be due to the presence of PCL in the sample which acts as nucleating agent. However, since the mass ratio between PCL and PLA polymers in all the prepared filaments is constant (mass PLA/mass PCL = 0.13(3), see Table S1), this decrease in T_{ccPLA} should be linked to the presence of the magnetic particles. In fact, the presence of NPs in the polymers is also shown as nucleation centers for the polymer crystallization [63]. Consequently, the interaction between NPs and PLA would minimize the polymer chain mobility, causing the crystallization process at lower temperatures. Although the used PLA has a higher molecular mass, it does not have the characteristic aliphatic chain of PCL that provides higher thermal stability to this last polymer. Thus, PCL is more stable to the change of environment of the polymer chains in the presence of other polymers or inorganic compounds and particles, while PLA is more unstable.

Fig. 4 **a** Crystallization of PCL in the 2nd cooling DSC curve, **b** melting of PCL, crystallization, and melting of PLA in the 2nd heating DSC curves for the series of magnetic filaments

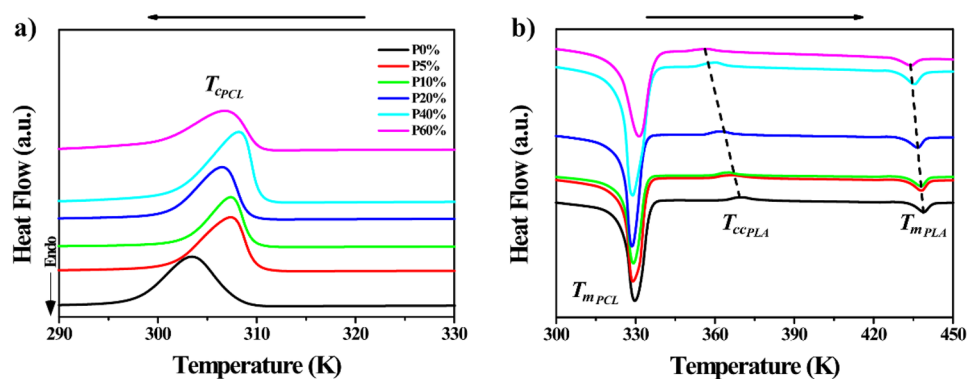


Table 2 Characteristic thermal parameters obtained from the DSC scans: cold crystallization temperature (T_{cc}), crystallization enthalpy (ΔH_{cc}), melting temperature (T_m), melting enthalpy (ΔH_m), and crystallinity degree (χ_c)

| Composite | PLA | | | | | PCL | | | | |
|-----------|--------------|--------------------------------------|-----------|-----------------------------------|--------------|-----------|-----------------------------------|-----------|-----------------------------------|--------------|
| | T_{cc} (K) | ΔH_{cc} (J·g ⁻¹) | T_m (K) | ΔH_m (J·g ⁻¹) | χ_c (%) | T_c (K) | ΔH_c (J·g ⁻¹) | T_m (K) | ΔH_m (J·g ⁻¹) | χ_c (%) |
| P0% | 370.5 | 35.2 | 438.9 | 23.0 | 13.1 | 303.4 | 68.8 | 329.7 | 66.0 | 56.5 |
| P5% | 365.5 | 25.5 | 437.9 | 47.4 | 23.4 | 307.1 | 63.9 | 329.0 | 68.0 | 58.3 |
| P10% | 364.9 | 25.7 | 437.3 | 43.8 | 19.4 | 306.3 | 69.1 | 329.0 | 72.2 | 62.6 |
| P20% | 362.2 | 16.9 | 435.5 | 37.1 | 24.5 | 307.0 | 69.9 | 328.9 | 59.1 | 51.3 |
| P40% | 359.9 | 22.8 | 435.2 | 46.1 | 24.9 | 308.2 | 67.9 | 328.7 | 69.5 | 60.0 |
| P60% | 358.1 | 32.1 | 434.4 | 42.6 | 11.3 | 306.2 | 79.5 | 331.7 | 94.6 | 81.7 |

The DSC scans also allow the determination of the corresponding crystallization and melting enthalpies of both polymers. Table 2 includes ΔH_c and ΔH_m together with the crystalline degree χ_c obtained for the PLA and PLC from Eqs. 1 and 2, respectively. No clear variations can be detected in the enthalpy values and χ_c for both polymers with the NP concentrations, despite the decreasing trend in the crystallization and melting temperatures found for the PLA. It should be noted that the low amount of PLA in the samples could affect the calculation of both enthalpy values, and consequently the possible variations with the NPs filling factor masked by experimental error. Anyway, it can be concluded that the introduction of the magnetic NPs in the polymeric matrix influences its thermal properties, particularly the decomposition process of both polymers and the crystallization temperature of PLA.

The magnetic properties of the extruded filaments and the commercial particles were analyzed via the magnetic field (H)-dependent magnetization, $M(H)$, curves (hysteresis loops) at room (RT) and low (10 K) temperatures (see Fig. 5).

It can be observed that while the commercial particles present the expected saturation magnetization (magnetization at 60 kOe, M_{60kOe}) at RT ($M_{60kOe} = 80 \text{ emu/g}_{\text{NPs}}$) for bulk magnetite Fe_3O_4 [64], M_{60kOe} decreases as the NPs loading is increased in the magnetic composites (from 41 $\text{emu/g}_{\text{composite}}$ for sample P60% to 3 $\text{emu/g}_{\text{composite}}$ for P5%). This reduction is a direct consequence of the negligible magnetic response of both polymers ($M \approx 0$) and the fact that the displayed magnetization values are normalized to the total mass of the composite. Therefore, taking into account the experimental M_{60kOe} , the filling factor of each filament can be estimated through the ratio $M_{60kOe}(\text{composite})/M_{60kOe}(\text{Fe}_3\text{O}_4)$ [61]. These values are in good agreement with the previously estimated NPs filling factor through TGA (see Table 1). On the other hand, nearly zero values of the reduced remanence, R , and coercive field, H_C , are obtained at RT for all the series of composites. Interestingly, this behavior depicts slight differences in comparison with the commercial Fe_3O_4 NPs, rising R at 10 K as the NPs filling factor increases (see Table 3). This increment in R can be ascribed to the formation of

preferential magnetic orientations of the particles along the filament axis into the polymer composite with respect to the random distribution in the powder sample [65, 66]. Indeed, considering that commercial particles were measured on tightly randomly packed powder samples, the chain formation into the polymer composite could lead to an increase in R as a consequence of the occurrence of interparticle magnetostatics interactions [67–69].

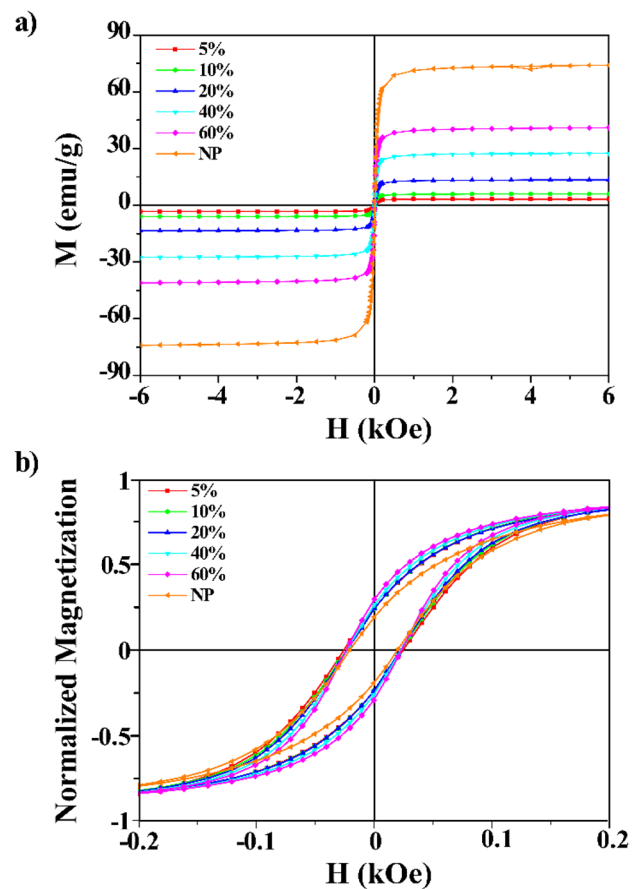
**Fig. 5** $M(H)$ curves at **a** RT and **b** low temperature (10 K) for all the series of composites. The magnetization at 10 K is normalized to the value at 60 kOe (M_{60kOe})

Table 3 Magnetic properties at RT and low temperature (10 K): M_{60kOe} , magnetization at 60 kOe; R , reduced magnetic remanence; H_C , coercive field. Maximum temperature, T_{max} , reached during the magnetic heating experiments in air and water, for all the series of composites

| Composite | Magnetic properties | | | | Heat-induced efficiency | | |
|-----------------------------------|---------------------|--|---------------------|------|-------------------------|---------------|---------------|
| | 300 K | | 10 K | | Air | Water | |
| | M_{60kOe} (emu/g) | | M_{60kOe} (emu/g) | R | H_C (Oe) | T_{max} (K) | T_{max} (K) |
| Fe ₃ O ₄ NP | 74 | | 83 | 0.18 | 202 | - | - |
| P5% | 3 | | 4 | 0.24 | 235 | 395 | 309 |
| P10% | 6 | | 7 | 0.24 | 232 | 452 | - |
| P20% | 13 | | 14 | 0.24 | 226 | 513 | 338 |
| P40% | 27 | | 31 | 0.26 | 230 | 632 | - |
| P60% | 41 | | 46 | 0.29 | 235 | 611 | 371 |

Due to their magnetic response, the as-prepared 3D printable filaments have the potential capability to act as localized heat sources activated by an externally applied AC magnetic field [70–72]. In order to test their heating capacity, the temperature of the different filaments was measured (magnetic hyperthermia experiments) under an AC magnetic field of 400 Oe (amplitude) and 311 kHz (frequency). Figure 6 shows the temperature evolution over time under the AC magnetic field when the filaments were in air (a) and (b) in water.

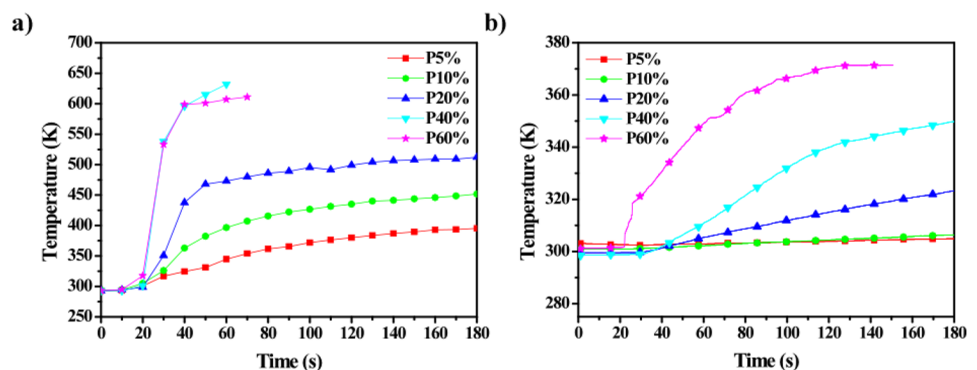
First, as can be observed in Fig. 6a, the temperature increases in all the filaments for very short periods of AC magnetic field exposure, i.e., 60 s. Afterwards, the filaments reach the thermal equilibrium, i.e., a maximum nearly constant temperature (T_{max}), when the generated heat by the NPs equals the outgoing heat flow to the environment. It is clearly shown that the heating capability under AC magnetic field arises from the presence of magnetic NPs in the composite as both the initial slope and T_{max} increase with the NPs filling factor. Interestingly, it should be noted that for high NPs loadings, i.e., 60%, the temperature reached at a very short exposition time increases above the decomposition temperature of the polymeric matrix and, thus, completely deteriorates the composite material. In addition, to prove the capability as heat generators in different environments, similar experiments were performed in aqueous media (see Fig. 6b). Although a comparable trend between

both experiments is observed, that is, larger heating with the increasing load of magnetic NPs, T_{max} is noticeably lower for water media due to the much higher specific heat capacity of water. In fact, only the sample P60% is able to reach the boiling point of water (373 K at 1 atm).

Finally, in order to fully characterize the heat-generating capability of the filaments, the specific absorption rate (SAR) and generated power density (ρ) values were obtained from the dynamic magnetization (from 13 to 553 Oe) measured at 311 kHz (Eqs. 3 and 4, respectively) in aqueous media. Figure 7 displays the estimated SAR as a function of the amplitude, H_{app} , of the applied magnetic field for the series of different filaments.

As it can be seen, the SAR values, normalized with the mass of NPs in the filament, are practically identical and independent of the NPs filling factor. Indeed, this is the expected behavior considering that the heat generated by the composites arises only from the magnetic NPs. However, sample P60% displays a slightly higher SAR value which can be linked to the higher remanence R detected in the previous magnetometry characterization. Although there are not many studies in the literature similar to our current study, the obtained SAR values are comparable to those previously published by other authors measured under similar conditions (see Table 4): for composites with similar [73] or smaller [74] NPs sizes.

Fig. 6 Temperature vs. time dependence for the filaments under an AC field of amplitude 400 Oe and $f=311$ kHz **a** in air and **b** in aqueous media



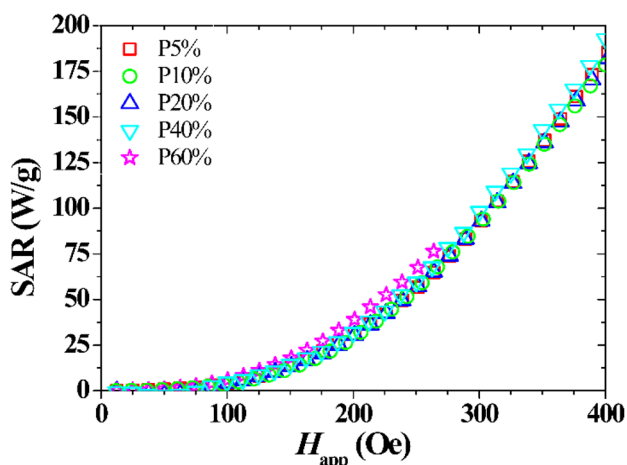


Fig. 7 SAR values of P5%, P10%, P20%, P40%, and P60% samples

Indeed, to corroborate the flexibility of the as-prepared magnetic filament, the maximum temperature increment (ΔT_{max}) achieved during the magnetic hyperthermia experiments (Fig. 7) is shown in Fig. 8a as a function of the generated power density (ρ). Moreover, in order to compare the individual heating capabilities for each polymeric composition, the generated ρ as a function of H_{app} is depicted in Fig. 8b. As expected, ρ increases with H_{app} [75].

Figure 8 can be employed in the design of efficient heating filament elements. For instance, according to Fig. 8a, to produce a temperature increase of, i.e., 100 K, it is necessary to generate a ρ of 8.5 kW m^{-3} . This can be achieved as shown in Fig. 8b, employing 3 samples, P5%, P20%, and P60%, depending on the H_{app} applied in the experiment (100, 200, or 380 Oe, respectively). Similarly, for a fixed H_{app} , the power generated for each sample depends on the NPs filling factor, being higher as NPs present in the sample increase.

This clearly reveals the versatility of these materials, where selecting a desired filling factor in the filaments and suitable applied magnetic field frequency and amplitude, the heating

Fig. 8 Generated power density ρ as a function of a maximum temperature increment ΔT_{max} and b the applied magnetic field (H_{app})

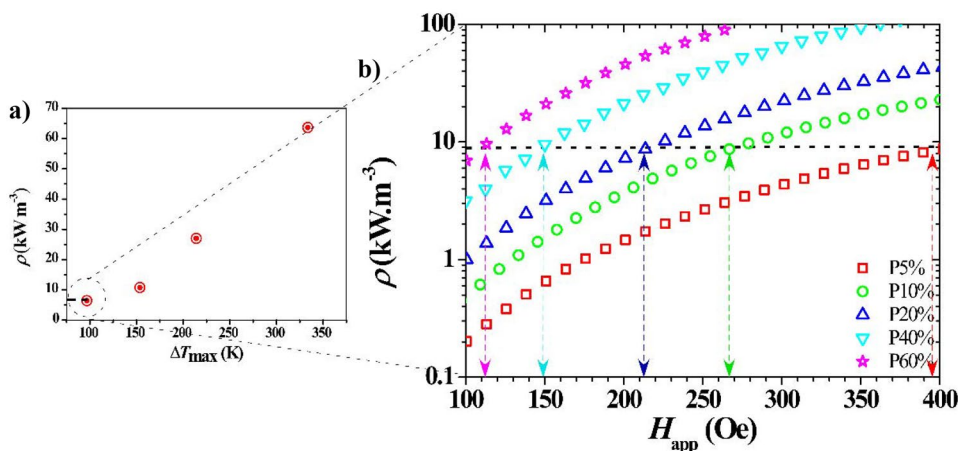


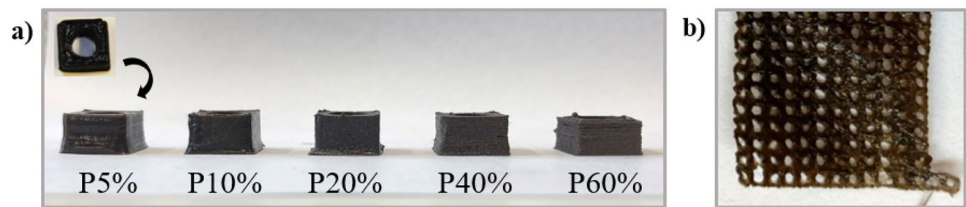
Table 4 Comparison between the measured SAR values for P5%, P20%, and P60% samples with other composites reported in the literature

| Material | SAR (W g^{-1}) | Frequency (KHz) | Magnetic field (Oe) | Ref |
|---|---------------------------|-----------------|---------------------|------|
| P5% | 30 | 311 | 200 | - |
| P20% | 32 | 311 | 200 | - |
| P60% | 39 | 311 | 200 | - |
| $\text{Fe}_3\text{O}_4/\text{MBG}/\text{PCL}$ | Up to 50 | 409 | 180 | [73] |
| Polysaccharide-derived hydrogels with Fe_3O_4 | 100–300 | 260 | 160 | [74] |

capacity can be adjusted to the needs of the user's application. For example, in medical applications, the H_{app} and f must not exceed a maximum limit ($H_{app} < 200\text{Oe}$ for $f=311 \text{ kHz}$) [76]. As it can be deduced from Fig. 8, in the safe region, a remarkable heating capacity can be achieved by selecting a filling factor above 5%, where the effective temperature could be also controlled through the exposure time (see Fig. 6). However, for other types of applications, such as controlled drug release [27], heterogeneous catalysis [33], water electrolysis [34], gas capture [35], or materials synthesis [77], the inductive heating generated falls on the necessity to overcome these limitations. Therefore, in these cases, filaments with high ρ as those as the magnetic composites herein presented can be envisaged as novel heat generators based on easy and low-cost manufacturing for FDM 3D printing technology.

Finally, the study is not complete if the printability of the prepared filaments is not clearly demonstrated. For this purpose, two different objects were printed: cubes of $10 \times 10 \times 10 \text{ mm}$ with a circular section hole of 5 mm employing all the set of composites (P5%—P60%) and a single $15 \times 40 \text{ mm}$ rectangular mesh with a $0.7 \times 0.8 \text{ mm}$ pattern using 10% nanoparticle loading (P10%) filament (see Fig. 9). In both cases, the printed objects show homogeneous and well-defined morphology corroborating the capability of the developed composites as novel easy manufacturing and economic magnetic raw material for FDM 3D printing technology.

Fig. 9 3D printed a cubic shape pieces and b mesh



4 Conclusions

In this study, we present the preparation of easy-manufacturing and low-cost magnetically active composites for raw materials for 3D printing technologies. The magnetic composite has been prepared by solution casting methodology mixing commercial Fe_3O_4 magnetic NPs embedded in a polymer mixture of PLA and PCL. The results reveal the possibility to extrude continuous and flexible magnetic filaments to be used in commercial 3D printers with variable NP-to-polymers compositions in the range of 5 to 60% in wt. While at low NPs concentrations, the filaments show a regular and dense structure, as the filling factor increases the filament becomes rougher with a consequent enhancement of the porosity. However, the NPs are well distributed along the whole structure independently of the NPs filling factor, and the increased porosity does not affect the macroscopic aspect of the extruded filament. Similarly, the thermal stability of the composite depends on the NPs loading, showing an overall reduction of the decomposition temperature of the polymeric blend as NPs filling increases. While the decomposition temperature decreases with the filling factor in both PLA and PCL polymers, only detectable changes in the melting and crystallization temperatures are found for the PLA. On the other hand, the inclusion of the magnetic NPs into the polymeric blend confers to the composite a magnetic response with saturation magnetization proportional to the NPs concentration. Taking advantage of the filament's magnetic character, their capability to generate heat under the application of low-frequency AC magnetic fields was analyzed. The composite can increase the temperature for very short periods (60 s) of AC magnetic field exposure (311 kHz and 400 Oe) in different environments. Lastly, the specific absorption rate (SAR) and absorbed power density (ρ) values were measured, obtaining 182 W g^{-1} and 45 kW m^{-3} maximum values at 311 kHz. These results expose the versatility of these easy manufacturing and low-cost filaments, where selecting a desired composition, the heating capacity can be adjusted to the needs of the user in applications where magnetic heat induction plays a key role such as magnetic hyperthermia, drug release, heterogeneous catalysis, water electrolysis, gas capture, or materials synthesis.

Supplementary Information The online version contains supplementary material available at <https://doi.org/10.1007/s42114-023-00687-4>.

Author contribution Jose Ignacio Pérez-Landazábal, Vicente Sanchez-Alarcos, and Vicente Recarte conceived this research and designed experiments. Itziar Galarreta-Rodriguez, Alberto Lopez-Ortega, Eneko Garayo, Cristina Gómez-Polo, and Jose Ignacio Pérez-Landazábal performed experiments, analysis, and interpretation of the data. All authors participated in the interpretation of the data. Itziar Galarreta-Rodriguez and Alberto Lopez-Ortega wrote the paper and participated in the revision of it. All authors read, revised, and approved the final manuscript.

Funding Open Access funding provided by Universidad Pública de Navarra. This work has been carried out with the financial support of the Navarra Government (project number PC017-018 AMELEC). The Spanish Government is acknowledged for the HIPERNANO research network (RED2018-102626-T). ALO acknowledges financial support from the grants PID2021-122613OB-I00 funded by MCIN/AEI/10.13039/501100011033 and PJUPNA2020 from Universidad Pública de Navarra. P. La Roca has received funding from “la Caixa” and “Caja Navarra” Foundations, under agreement LCF/PR/PR13/51080004.

Declarations

Conflict of interest The authors declare no competing interests.

Open Access This article is licensed under a Creative Commons Attribution 4.0 International License, which permits use, sharing, adaptation, distribution and reproduction in any medium or format, as long as you give appropriate credit to the original author(s) and the source, provide a link to the Creative Commons licence, and indicate if changes were made. The images or other third party material in this article are included in the article's Creative Commons licence, unless indicated otherwise in a credit line to the material. If material is not included in the article's Creative Commons licence and your intended use is not permitted by statutory regulation or exceeds the permitted use, you will need to obtain permission directly from the copyright holder. To view a copy of this licence, visit <http://creativecommons.org/licenses/by/4.0/>.

References

- Goh GD, Sing SL, Yeong WY (2021) A review on machine learning in 3D printing: applications, potential, and challenges. *Artif Intell Rev* 54:63–94. <https://doi.org/10.1007/S10462-020-09876-9>
- Zhang C, Li X, Jiang L, Tang D, Xu H, Zhao P, Fu J, Zhou Q, Chen Y (2021) 3D printing of functional magnetic materials: from design to applications. *Adv Funct Mater* 31:2102777. <https://doi.org/10.1002/ADFM.202102777>
- Revilla-León M, Özcan M (2019) Additive manufacturing technologies used for processing polymers: current status and potential application in prosthetic dentistry. *J Prosthodont* 28:146–158. <https://doi.org/10.1111/JOPR.12801>
- Ramazani H, Kami A (2022) Metal FDM, a new extrusion-based additive manufacturing technology for manufacturing of metallic parts: a review. *Prog Addit Manuf* 7:609–626. <https://doi.org/10.1007/S40964-021-00250-X/TABLES/5>

5. Lu Z, Cao J, Song Z, Li D, Lu B (2019) Research progress of ceramic matrix composite parts based on additive manufacturing technology. *Virtual Phys Prototyp* 14:333–348. <https://doi.org/10.1080/17452759.2019.1607759>
6. Popescu D, Zapciu A, Amza C, Baciu F, Marinescu R (2018) FDM process parameters influence over the mechanical properties of polymer specimens: a review. *Polym Test* 69:157–166. <https://doi.org/10.1016/J.POLYMERTESTING.2018.05.020>
7. Prabhakar MM, Saravanan AK, Lenin AH, Leno JJ, Mayandi K, Ramalingam PS (2021) A short review on 3D printing methods, process parameters and materials. *Mater Today Proc* 45:6108–6114. <https://doi.org/10.1016/J.MATPR.2020.10.225>
8. Wong JY (2015) Ultra-portable solar-powered 3D printers for onsite manufacturing of medical resources. *Aerosp Med Hum Perform* 86:830–834. <https://doi.org/10.3357/AMHP.4308.2015>
9. Loh GH, Pei E, Harrison D, Monzón MD (2018) An overview of functionally graded additive manufacturing. *Addit Manuf* 23:34–44. <https://doi.org/10.1016/J.ADDMA.2018.06.023>
10. Jiang Q, Qiao Y, Xiang C, Uddin A, Wu L, Qin F (2022) Meta-composite based on three-dimensional ferromagnetic microwave architecture for electromagnetic response. *Adv Compos Hybrid Mater* 5:3190–3200. <https://doi.org/10.1007/S42114-021-00394-Y/METRICS>
11. Gao T, Rong H, Mahmoud KH, Ruan J, El-Bahy SM, Faheim AA, Li Y, Huang M, Nassan MA, Zhao R (2022) Iron/silicon carbide composites with tunable high-frequency magnetic and dielectric properties for potential electromagnetic wave absorption. *Adv Compos Hybrid Mater* 5:1158–1167. <https://doi.org/10.1007/S42114-022-00507-1/METRICS>
12. Rajak DK, Pagar DD, Kumar R, Pruncu CI (2019) Recent progress of reinforcement materials: a comprehensive overview of composite materials. *J Mater Res Technol* 8:6354–6374. <https://doi.org/10.1016/J.JMRT.2019.09.068>
13. Cooperstein I, Sachyani-Keneth E, Shukrun-Farrell E, Rosental T, Wang X, Kamyshny A, Magdassi S (2018) Hybrid materials for functional 3D printing. *Adv Mater Interfaces* 5:1800996. <https://doi.org/10.1002/ADMI.201800996>
14. Xu P, Huang B, Tang R, Wang Z, Tu J, Ding Y (2022) Improved mechanical and EMI shielding properties of PLA/PCL composites by controlling distribution of PIL-modified CNTs. *Adv Compos Hybrid Mater* 5:991–1002. <https://doi.org/10.1007/S42114-021-00406-X/TABLES/1>
15. Jia Z, Zhang X, Gu Z, Wu G (2023) MOF-derived Ni-Co bimetal/porous carbon composites as electromagnetic wave absorber. *Adv Compos Hybrid Mater* 6:1–12. <https://doi.org/10.1007/s42114-022-00615-y>
16. Ren X, Song Y, Gao Z, Wu Y, Jia Z, Wu G (2023) Rational manipulation of composition and construction toward Zn/Co bimetal hybrids for electromagnetic wave absorption. *J Mater Sci Technol* 134:254–261. <https://doi.org/10.1016/j.jmst.2022.07.004>
17. Liu Y, Zhou X, Jia Z, Wu H, Wu G (2022) Oxygen vacancy-induced dielectric polarization prevails in the electromagnetic wave-absorbing mechanism for Mn-based MOFs-derived composites. *Adv Funct Mater* 32. <https://doi.org/10.1002/adfm.202204499>
18. Shokrollahi H, Janghorban K (2007) Soft magnetic composite materials (SMCs). *J Mater Process Technol* 189:1–12. <https://doi.org/10.1016/J.JMATPROTEC.2007.02.034>
19. Xie X, Gao H, Luo X, Zhang Y, Qin Z, Ji H (2022) Polyethyleneimine-modified magnetic starch microspheres for Cd(II) adsorption in aqueous solutions. *Adv Compos Hybrid Mater* 5:2772–2786. <https://doi.org/10.1007/S42114-022-00422-5/METRICS>
20. Shao Y, Bai H, Wang H, Fei G, Li L, Zhu Y (2022) Magnetically sensitive and high template affinity surface imprinted polymer prepared using porous TiO₂-coated magnetite-silica nanoparticles for efficient removal of tetrabromobisphenol A from polluted water. *Adv Compos Hybrid Mater* 5:130–143. <https://doi.org/10.1007/S42114-021-00361-7/METRICS>
21. Yang Y, Song X, Li X, Chen Z, Zhou C, Zhou Q, Chen Y, Yang Y, Li X, Chen Y, Song X, Chen Z, Zhou Q, Zhou C (2018) Recent progress in biomimetic additive manufacturing technology: from materials to functional structures. *Adv Mater* 30:1706539. <https://doi.org/10.1002/ADMA.201706539>
22. Ngo TD, Kashani A, Imbalzano G, Nguyen KTQ, Hui D (2018) Additive manufacturing (3D printing): a review of materials, methods, applications and challenges. *Compos Part B Eng* 143:172–196. <https://doi.org/10.1016/J.COMPOSITESB.2018.02.012>
23. Du W, Ren X, Pei Z, Ma C (2020) Ceramic binder jetting additive manufacturing: a literature review on density. *J Manuf Sci Eng Trans ASME* 142. <https://doi.org/10.1115/1.4046248/1074276>
24. Cullity BD, Graham CD (2009) Introduction to magnetic materials, 2nd edn. John Wiley & Sons, Hoboken, New Jersey
25. Lian Y, Wang L, Cao J, Liu T, Xu Z, Yang B, Huang T, Jiang X, Wu N (2021) Recent advances on the magnetic nanoparticle-based nanocomposites for magnetic induction hyperthermia of tumor: a short review. *Adv Compos Hybrid Mater* 4:925–937. <https://doi.org/10.1007/S42114-021-00373-3/METRICS>
26. Wang X, Qi Y, Hu Z, Jiang L, Pan F, Xiang Z, Xiong Z, Jia W, Hu J, Lu W (2022) Fe₃O₄@PVP@DOX magnetic vortex hybrid nanostructures with magnetic-responsive heating and controlled drug delivery functions for precise medicine of cancers. *Adv Compos Hybrid Mater* 5:1786–1798. <https://doi.org/10.1007/S42114-022-00433-2/METRICS>
27. García L, Garaio E, López-Ortega A, Galarreta-Rodríguez I, Cervera-Gabalda L, Cruz-Quesada G, Cornejo A, Garrido JJ, Gómez-Polo C, Pérez-Landazábal JI (2022) Fe₃O₄-SiO₂ mesoporous core/shell nanoparticles for magnetic field-induced ibuprofen-controlled release. *Langmuir*. <https://doi.org/10.1021/ACS.LANGMUIR.2C02408>
28. Galarreta-Rodríguez I, Marciano L, Castellanos-Rubio I, Gil De Muro I, García I, Olivi L, Fernández-Gubieda ML, Castellanos-Rubio A, Lezama L, De Larramendi IR, Insausti M (2022) Towards the design of contrast-enhanced agents: systematic Ga³⁺ doping on magnetite nanoparticles. *Dalt Trans* 51:2517–2530. <https://doi.org/10.1039/D1DT03029A>
29. Stella B, Arpicco S, Peracchia MT, Desmaële D, Hoebeke J, Renoir M, D'Angelo J, Cattel L, Couvreur P (2000) Design of folic acid-conjugated nanoparticles for drug targeting. *J Pharm Sci* 89:1452–1464. [https://doi.org/10.1002/1520-6017\(200011\)89:11%3c1452::aid-jps8%3e3.0.co;2-p](https://doi.org/10.1002/1520-6017(200011)89:11%3c1452::aid-jps8%3e3.0.co;2-p)
30. Rügenapp C, Gleich B, Haase A (2012) Magnetic nanoparticles in magnetic resonance imaging and diagnostics. *Pharm Res* 29:1165–1179. <https://doi.org/10.1007/S11095-012-0711-Y>
31. Périgo EA, Hemery G, Sandre O, Ortega D, Garaio E, Plazaola F, Teran FJ (2015) Fundamentals and advances in magnetic hyperthermia. *Appl Phys Rev* 2:041302. <https://doi.org/10.1063/1.4935688>
32. Guo Y, Zhang Y, Ma J, Li Q, Li Y, Zhou X, Zhao D, Song H, Chen Q, Zhu X (2018) Light/magnetic hyperthermia triggered drug released from multi-functional thermo-sensitive magnetoliposomes for precise cancer synergetic theranostics. *J Control Release* 272:145–158. <https://doi.org/10.1016/J.JCONREL.2017.04.028>
33. Yassine SR, Fatfat Z, Darwish GH, Karam P (2020) Localized catalysis driven by the induction heating of magnetic nanoparticles. *Catal Sci Technol* 10:3890–3896. <https://doi.org/10.1039/D0CY00439A>
34. Seo B, Joo SH (2018) A magnetic boost. *Nat Energy* 3(3):451–452. <https://doi.org/10.1038/s41560-018-0157-5>
35. Sadiq MM, Li H, Hill AJ, Falcaro P, Hill MR, Suzuki K (2016) Magnetic induction swing adsorption: an energy efficient route to porous adsorbent regeneration. *Chem Mater* 28:6219–6226. https://doi.org/10.1021/ACS.CHEMMATER.6B02409/ASSET/IMAGES/LARGE/CM-2016-02409G_0009.JPEG

36. Gómez-Polo C, Larumbe S, Barquín LF, Fernández LR (2016) Magnetic induction heating as a new tool for the synthesis of Fe₃O₄-TiO₂ nanoparticle systems. *J Nanoparticle Res* 18:1–9. <https://doi.org/10.1007/S11051-016-3426-X/FIGURES/5>
37. Zhang Y, Zhai D, Xu M, Yao Q, Chang J, Wu C (2016) 3D-printed bioceramic scaffolds with a Fe₃O₄/graphene oxide nanocomposite interface for hyperthermia therapy of bone tumor cells. *J Mater Chem B* 4:2874–2886. <https://doi.org/10.1039/C6TB00390G>
38. Jackson RJ, Patrick PS, Page K, Powell MJ, Lythgoe MF, Miodownik MA, Parkin IP, Carmalt CJ, Kalber TL, Bear JC (2018) Chemically treated 3D printed polymer scaffolds for biomineral formation. *ACS Omega* 3:4342–4351. https://doi.org/10.1021/ACSSOMEGA.8B00219/ASSET/IMAGES/LARGE/AO-2018-00219J_0008.JPEG
39. Tang J, Yin Q, Shi M, Yang M, Yang H, Sun B, Guo B, Wang T (2021) Programmable shape transformation of 3D printed magnetic hydrogel composite for hyperthermia cancer therapy. *Extrem Mech Lett* 46:101305. <https://doi.org/10.1016/J.EML.2021.101305>
40. Saiter A, Delpouve N, Dargent E, Saiter JM (2007) Cooperative rearranging region size determination by temperature modulated DSC in semi-crystalline poly(L-lactide acid). *Eur Polym J* 43:4675–4682. <https://doi.org/10.1016/J.EURPOLYMJ.2007.07.039>
41. Lovell CS, Fitz-Gerald JM, Park C (2011) Decoupling the effects of crystallinity and orientation on the shear piezoelectricity of polylactic acid. *J Polym Sci Part B Polym Phys* 49:1555–1562. <https://doi.org/10.1002/POLB.22345>
42. Blázquez-Blázquez E, Pérez E, Lorenzo V, Cerrada ML (2019) Crystalline characteristics and their influence in the mechanical performance in poly(ϵ -caprolactone) / high density polyethylene blends. *Polym* 2019:11. <https://doi.org/10.3390/POLYM11111874>
43. Guarino V, Cirillo V, Taddei P, Alvarez-Perez MA, Ambrosio L (2011) Tuning size scale and crystallinity of PCL electrospun fibres via solvent permittivity to address hMSC response. *Macromol Biosci* 11:1694–1705. <https://doi.org/10.1002/MABI.201100204>
44. Suryanegara L, Nakagaito AN, Yano H (2009) The effect of crystallization of PLA on the thermal and mechanical properties of microfibrillated cellulose-reinforced PLA composites. *Compos Sci Technol* 69:1187–1192. <https://doi.org/10.1016/j.compscitech.2009.02.022>
45. PCE–Infrared Thermography Mod.PCE-TC 33N. Available online: https://www.pce-instruments.com/espanol/instrumento-medida/medidor/camara-termografica-pce-instruments-c_mara-termogr_fica-pce-tc-33n-det_5930746.htm. Accessed 26 Sep 2022
46. Garaio E, Collantes JM, Plazaola F, Garcia JA, Castellanos-Rubio I (2014) A multifrequency electromagnetic applicator with an integrated AC magnetometer for magnetic hyperthermia experiments. *Meas Sci Technol* 25:115702. <https://doi.org/10.1088/0957-0233/25/11/115702>
47. Rosensweig RE (2002) Heating magnetic fluid with alternating magnetic field. *J Magn Magn Mater* 252:370–374. [https://doi.org/10.1016/S0304-8853\(02\)00706-0](https://doi.org/10.1016/S0304-8853(02)00706-0)
48. Gómez-Polo C, Recarte V, Cervera L, Beato-López JJ, López-García J, Rodríguez-Velamazán JA, Ugarte MD, Mendonça EC, Duque JGS (2018) Tailoring the structural and magnetic properties of Co-Zn nanosized ferrites for hyperthermia applications. *J Magn Magn Mater* 465:211–219. <https://doi.org/10.1016/j.jmmm.2018.05.051>
49. Pennes HH (1948) Analysis of tissue and arterial blood temperatures in the resting human forearm. *J Appl Physiol* 1:93–122. <https://doi.org/10.1152/jappl.1948.1.2.93>
50. Fortelny I, Ujčić A, Fambri L, Slouf M (2019) Phase structure, compatibility, and toughness of PLA/PCL blends: a review. *Front Mater* 6:1–13. <https://doi.org/10.3389/fmats.2019.00206>
51. Takayama T, Todo M, Tsuji H (2011) Effect of annealing on the mechanical properties of PLA/PCL and PLA/PCL/LTI polymer blends. *J Mech Behav Biomed Mater* 4:255–260. <https://doi.org/10.1016/j.jmbbm.2010.10.003>
52. Senatov FS, Niaza KV, Zadorozhnyy MY, Maksimkin AV, Kaloshkin SD, Estrin YZ (2016) Mechanical properties and shape memory effect of 3D-printed PLA-based porous scaffolds. *J Mech Behav Biomed Mater* 57:139–148. <https://doi.org/10.1016/J.JMBBM.2015.11.036>
53. Luis Ordóñez Avila J, Elena Perdomo M, Yanire Rivas Bejarano M, Luis Ordóñez Fernández J (2021) Mechanical displacement for 3D printers' parts using FEM as inverse engineering method in Honduras. *J Phys Conf Ser* 1877:012013. <https://doi.org/10.1088/1742-6596/1877/1/012013>
54. Tanzli E, Ehrmann A (2021) Electrospun nanofibrous membranes for tissue engineering and cell growth. *Appl Sci* 11:6929. <https://doi.org/10.3390/APP11156929>
55. Wang G, Yang S, Wei Z, Dong X, Wang H, Qi M (2013) Facile preparation of poly(ϵ -caprolactone)/Fe₃O₄@graphene oxide superparamagnetic nanocomposites. *Polym Bull* 70:2359–2371. <https://doi.org/10.1007/S00289-013-0957-5>
56. Yang R (2020) Polymer degradation and stability. *Polym Sci Nanotechnol Fundam Appl* 125–148. <https://doi.org/10.1016/B978-0-12-816806-6.00007-8>
57. Xue W, Hu Y, Wang F, Yang X, Wang L (2019) Fe₃O₄/poly(caprolactone) (PCL) electrospun membranes as methylene blue catalyst with high recyclability. *Colloids Surfaces A Physicochem Eng Asp* 564:115–121. <https://doi.org/10.1016/J.COLSURFA.2018.12.037>
58. Yu B, Wang M, Sun H, Zhu F, Han J, Bhat G (2017) Preparation and properties of poly (lactic acid)/ magnetic Fe₃O₄ composites and nonwovens. <https://doi.org/10.1039/c7ra06427f>
59. Luyt AS, Gasmi S (2016) Influence of blending and blend morphology on the thermal properties and crystallization behaviour of PLA and PCL in PLA/PCL blends. *J Mater Sci* 51:4670–4681. <https://doi.org/10.1007/s10853-016-9784-z>
60. Finotti PFM, Costa LC, Chinelatto MA (2016) Effect of the chemical structure of compatibilizers on the thermal, mechanical and morphological properties of immiscible PLA/PCL blends. *Macromol Symp* 368:24–29. <https://doi.org/10.1002/masy.201600056>
61. Nájera SE, Michel M, Kim NS (2018) Characterization of 3D Printed PLA/PCL/TiO₂ Composites for Cancellous Bone. *J Mater Sci Eng* 7:417. <https://doi.org/10.4172/2169-0022.1000417>
62. Navarro-Baena I, Sessini V, Dominici F, Torre L, Kenny JM, Peponi L (2016) Design of biodegradable blends based on PLA and PCL: from morphological, thermal and mechanical studies to shape memory behavior. *Polym Degrad Stab* 132:97–108. <https://doi.org/10.1016/J.POLYMDEGRADSTAB.2016.03.037>
63. Fortunati E, Armentano I, Zhou Q, Puglì D, Terenzi A, Berglund LA, Kenny JM (2012) Microstructure and nonisothermal cold crystallization of PLA composites based on silver nanoparticles and nanocrystalline cellulose. *Polym Degrad Stab* 97:2027–2036. <https://doi.org/10.1016/J.POLYMDEGRADSTAB.2012.03.027>
64. Cullity BD, Bernard D (1972) Introduction to magnetic materials. Addison-Wesley Pub. Co., Reading, Mass
65. Gavilán H, Simeonidis K, Myrovali E, Mazarío E, Chubykalo-Fesenko O, Chantrell R, Balcells L, Angelakeris M, Morales MP, Serantes D (2021) How size, shape and assembly of magnetic nanoparticles give rise to different hyperthermia scenarios. *Nanoscale* 13:15631–15646. <https://doi.org/10.1039/D1NR03484G>
66. Eloi JC, Okuda M, Correia Carreira S, Schwarzacher W, Correia MJ, Figueiredo W (2014) Effective energy barrier distributions for random and aligned magnetic nanoparticles. *J Phys Condens Matter* 26:146006. <https://doi.org/10.1088/0953-8984/26/14/146006>
67. Myrovali E, Papadopoulos K, Iglesias I, Spasova M, Farle M, Wiedwald U, Angelakeris M (2021) Long-range ordering effects in magnetic nanoparticles. *Cite This ACS Appl Mater Interfaces* 13:21602–21612. <https://doi.org/10.1021/acsami.1c01820>

68. Simeonidis K, Puerto Morales M, Marciello M, Angelakeris M, De La Presa P, Lazaro-Carrillo A, Tabero A, Villanueva A, Chubykalo-Fesenko O, Serantes D (2016) In-situ particles reorientation during magnetic hyperthermia application: Shape matters twice OPEN. *Sci Rep* 6:38382. <https://doi.org/10.1038/srep38382>
69. Prozorov R, Prozorov T, Mallapragada SK, Narasimhan B, Williams TJ, Bazylinski DA (2007) Magnetic irreversibility and the Verwey transition in nanocrystalline bacterial magnetite. *Phys Rev B* 76:054406. <https://doi.org/10.1103/PhysRevB.76.054406>
70. Martinez-Boubeta C, Simeonidis K, Makridis A, Angelakeris M, Iglesias O, Guardia P, Cabot A, Yedra L, Estradé S, Peiró F, Saghi Z, Midgley PA, Conde-Leborán I, Serantes D, Baldomir D (2013) Learning from nature to improve the heat generation of iron-oxide nanoparticles for magnetic hyperthermia applications. *Sci Reports* 31(3):1–8. <https://doi.org/10.1038/srep01652>
71. Nemati Z, Alonso J, Rodrigo I, Das R, Garaio E, García JA, Orue I, Phan MH, Srikanth H (2018) Improving the heating efficiency of iron oxide nanoparticles by tuning their shape and size. *J Phys Chem C* 122:2367–2381. https://doi.org/10.1021/ACS.JPCC.7B10528/SUPPL_FILE/JP7B10528_SI_001.PDF
72. Garaio E, Sandre O, Collantes JM, Garcia JA, Mornet S, Plazaola F (2014) Specific absorption rate dependence on temperature in magnetic field hyperthermia measured by dynamic hysteresis losses (ac magnetometry). *Nanotechnology* 26:015704. <https://doi.org/10.1088/0957-4484/26/1/015704>
73. Zhang J, Zhao S, Zhu M, Zhu Y, Zhang Y, Liu Z, Zhang C (2014) 3D-printed magnetic Fe₃O₄/MBG/PCL composite scaffolds with multifunctionality of bone regeneration, local anticancer drug delivery and hyperthermia. *J Mater Chem B* 2:7583–7595. <https://doi.org/10.1039/C4TB01063A>
74. Hernández R, Sacristán J, Asín L, Torres TE, Ibarra MR, Goya GF, Mijangos C (2010) Magnetic hydrogels derived from polysaccharides with improved specific power absorption: potential devices for remotely triggered drug delivery. *J Phys Chem B* 114:12002–12007. https://doi.org/10.1021/JP105556E/ASSET/IMAGES/LARGE/JP-2010-05556E_0007.JPEG
75. Andrä W, d'Ambly CG, Hergt R, Hilger I, Kaiser WA, Andrä W, d'Ambly CG, Hergt R, Hilger I, Kaiser WA (1999) Temperature distribution as function of time around a small spherical heat source of local magnetic hyperthermia. *JMMM* 194:197–203. [https://doi.org/10.1016/S0304-8853\(98\)00552-6](https://doi.org/10.1016/S0304-8853(98)00552-6)
76. Hergt R, Dutz S, Hergt R, Dutz S (2007) Magnetic particle hyperthermia—biophysical limitations of a visionary tumour therapy. *JMMM* 311:187–192. <https://doi.org/10.1016/J.JMMM.2006.10.1156>
77. Cervera L, Pérez-Landazábal JI, Garaio E, Monteserín M, Larumbe S, Martín F, Gómez-Polo C (2021) Fe-C nanoparticles obtained from thermal decomposition employing sugars as reducing agents. *J Alloys Compd* 863:158065. <https://doi.org/10.1016/J.JALLCOM.2020.158065>

Publisher's Note Springer Nature remains neutral with regard to jurisdictional claims in published maps and institutional affiliations.